Key Points:
- Dry granular slide experiments have been conducted in three laboratory Froude number scale series
- The laboratory slides showed scale effects strongly dependent on the grain Reynolds number
- Discrete element method (DEM) simulations without air failed to capture these scale effects

Correspondence to:
M. Kesseler,
mattkesseler1@gmail.com

Grain Reynolds Number Scale Effects in Dry Granular Slides

Matthew Kesseler[1], Valentin Heller[1], and Barbara Turnbull[1]

[1]Environmental Fluid Mechanics and Geoprocesses Research Group, Faculty of Engineering, University of Nottingham, Nottingham, UK

Abstract Scale effects are differences in physical behavior that manifest between a large event and a geometrically scaled laboratory model and may cause misleading predictions. This study focuses on scale effects in granular slides, important in the environment and to industry. A versatile 6 m long laboratory setup has been built following Froude similarity to investigate dry granular slides at scales varied by a factor of 4, with grain Reynolds numbers Re in the range of 10^2 to 10^3. To provide further comparison, discrete element method simulations have also been conducted. Significant scale effects were identified; the nondimensional surface velocity increased by up to 35%, while the deposit runout distance increased by up to 26% from the smallest to the largest model. These scale effects are strongly correlated with Re, suggesting that interactions between grains and air are primarily responsible for the observed scale effects. This is supported by the discrete element method data, which did not show these scale effects in the absence of air. Furthermore, the particle drag force accounted for a significant part of the observed scale effects. Cauchy number scale effects caused by unscaled particle stiffness resulting in varying dust formation with scale are found to be of secondary importance. Comparisons of the laboratory data to that of other studies and of natural events show that data normalization with Re is an effective method of quantitatively comparing laboratory results to natural events. This upscaling technique can improve hazard assessment in nature and is potentially useful for modeling industrial flows.

1. Introduction

Granular slides and flows are omnipresent, occurring in natural conditions such as rockfalls, landslides, pyroclastic flows, and avalanches (Pudasaini & Hutter, 2010), and in industrial contexts including heap development (Bryant et al., 2014; Markauskas & Kačianauskas, 2011; Zhang & Vu-Quoc, 2000), chutes, hoppers, rotating drums, and blenders (Turnbull, 2011; Zhu et al., 2008). They can be identified as collections of individual particles moving in unison, with the space between particles being filled with an interstitial fluid (Campbell, 2006). This study focuses on dry granular slides, where the interstitial fluid is air. Granular slides differ from continuous flows by having defined initial, transient, and final states. These are typically triggered by direct mechanical action, temperature changes of the solid or fluid phase, or acoustic propagation (Aradian et al., 2002; Juanico et al., 2008).

Landslides and avalanches can be extremely massive and influence large areas (Xu et al., 2014), causing considerable damage during their passing (Haque et al., 2016) and resulting in indirect effects such as tsunamis or artificial dam formation (Heller et al., 2008; Kelfoun et al., 2010; Walsh et al., 2012). The relevance of granular events and the challenge to measure them in nature justify the use of scaled experiments to develop understanding of their physical processes, facilitating more repeatable and detailed analysis in a cost-effective manner. The sheer scale of natural events makes controlled physical experiments of comparable dimensions (Iverson et al., 2010; McElwaine & Nishimura, 2001; Moriwaki et al., 2004) rather rare.

While physical modeling is useful for capturing key physical mechanisms, model effects can be caused by misrepresentation of features secondary to the model's focus, such as the terrain, materials, or slide initiation mechanisms. Additionally, measurement effects can be caused by differences in measurement techniques between natural events and models. While these two effects can be readily corrected in principle, scale effects are much harder to isolate and account for. Many key parameters of a phenomenon scale nonlinearly and independently of each other; as a result, it is practically impossible to correctly scale all involved parameters and completely avoid scale effects (Heller, 2011).

Scale effects are produced when force ratios observed in nature vary from those in a scaled model. In granular slides, the Froude number (Fr), corresponding to the ratio of inertial and gravity forces, dominates slide motion in comparison to other force ratios (Choi et al., 2015). Fr is defined as

$$Fr = \frac{U}{\sqrt{gL}}, \tag{1}$$

where U and L are characteristic velocity and length scales and g is the gravitational acceleration. The grain Reynolds number (Re) is also highly relevant to granular slides (Iverson, 1997; Zhou & Ng, 2010) and is the ratio between the inertial and viscous forces of the surrounding media acting on a single particle. Re is defined as

$$Re = \frac{UL}{\nu_f}, \tag{2}$$

with ν_f being the kinematic fluid viscosity, and quantifies whether the drag force acting on these individual particles is primarily laminar or turbulent. Re is the most relevant Reynolds number for evaluating slide dynamics as the fluid flow around individual particles depends more strongly on the particle shape and local granular system than on the granular slide as a whole. Additionally, the Cauchy number (Ca) relates to the ratio of inertial and elastic forces acting on particles during collisions. Ca is defined as

$$Ca = \frac{\rho_g U^2}{E}, \tag{3}$$

with ρ_g being the particle density, and E being the particle Young's modulus, and Ca is also potentially relevant to granular slides (Heller, 2011). Each of the force ratios in equations (1)–(3) follows different scaling laws, preventing full similarity of key slide parameters across all force ratios.

A scale series of granular slides can be constructed such that Fr is kept constant between scales (Heller et al., 2008; Kesseler et al., 2018). This eliminates the gravity force as a cause of scale effects, such that they are primarily due to differences in Re and other force ratios such as Ca. Sometimes phenomena are self-similar and Froude scaling completely models them without significant scale effects, and others may be Re-invariant without significant Re-dependent scale effects (Heller, 2017). Identifying which key parameters of granular slides are Re-invariant and which are not (and thus show scale effects) would be highly useful for comparing slide data from different scales.

Granular dynamics has seen relatively little focus on scale effects (Iverson, 2015) in contrast to experimental fluid dynamics (Heller, 2011), with the scale separation between macroscopic slide and microscopic particle scales remaining unclear (Andreotti et al., 2013; Armanini, 2013). Furthermore, granular systems have many additional properties that increase the complexity of their scaling compared to fluid systems, such as particle fracture, stress anisotropy, and local and historical effects. Bowman et al. (2012) and Ng et al. (2018), for example, focus on the influence of particle fracture on slide dynamics, using centrifuges to produce fracturing stress levels at small scales and identifying that particle fracture can significantly influence slide runout distance and impact force, respectively. Granular systems thus have a wider range of variables and constraints that must be controlled to ensure proper scaling throughout the slide duration (Slonaker et al., 2017). Many studies looking at granular scaling focus on comparing the macroscales and microscales (Brodu et al., 2015; Bryant et al., 2014; Slonaker et al., 2017), or relative scales within an event (Warnett et al., 2014), rather than comparing geometrically similar systems at different sizes (Iverson, 2015). Additionally, other studies focus on scale effects in the surrounding fluid rather than in the granular systems themselves (Ettema et al., 2006; Heller et al., 2008; Ranieri, 2007), with studies investigating scale effects in granular systems typically focusing on continuous flows rather than discrete granular slides (Artoni et al., 2012; Pouliquen, 1999).

Furthermore, scale effects addressed in this work are not necessarily relevant to size effects such as hyper-mobility that have been more thoroughly studied (Johnson et al., 2016; Parez & Aharonov, 2015). Size effects typically occur once a discrete volume threshold is passed, and do not strictly relate to differences in force ratios such as equations (1)–(3) or other stress ratios in Iverson (1997). For example, hypermobility is a size effect observed as a drastic increase in runout distance, for example, in slides over 10^6 m^3, unrelated to gradual changes in runout distance below this threshold as for scale effects. While some suggest that size effects are caused solely by the physics of a granular system in isolation (Parez & Aharonov, 2015), others suggest

that secondary mechanisms such as lubrication, fluidization, and velocity frictional weakening are responsible (Collins & Melosh, 2003; Davies & McSaveney, 1999; Erismann, 1986; Savage & Hutter, 1989), which match the definition of model effects better than of scale effects. The field of scale effects in granular slides is thus relatively unexplored.

The discrete element method (DEM), introduced by Cundall and Strack (1979) to the field of granular systems, has developed significantly over the last few decades as a powerful numerical technique for modeling dense granular flows. Poschel (1993) first applied the DEM to inclined chute flows and Zhu et al. (2008) reviews applications of the DEM to a range of granular flow contexts. The DEM complements physical modeling well, as difficult-to-control parameters such as the friction angle and restitution coefficient can be implemented directly. A major advantage of the DEM in comparison to continuum-based approaches including depth-averaged models (Savage & Hutter, 1989), the material point method (Llano-Serna et al., 2016), and smoothed particle hydrodynamics (Nguyen et al., 2017), is its direct capture of particle-scale interactions. While the DEM typically uses spherical particles for improved performance, rolling-resistance modeling can be applied to better represent the energy of systems of rough particles (Ai et al., 2011; Wensrich & Katterfeld, 2012), while multisphere clumps can be used to capture shape effects more precisely if required (Kruggel-Emden et al., 2008). This allows the DEM to better represent phenomena specifically linked to particle characteristics including size, shape, and relative displacement of particles, such as size segregation, slide dilation and contraction, contact force transference, and jamming events. In this study, spherical particles are used with a rolling-resistance model to allow for timely simulation of laboratory experiments.

This study primarily aims to quantify the relative importance of Re in the scale effects identified in the laboratory data set. The overall data set consists of laboratory and numerical data at three different experimental scales and three initial conditions at each scale, adopting and improving on the methodology in Kesseler et al. (2018). Key slide parameters were nondimensionalized and compared, showcasing the match of the DEM simulations to the corresponding laboratory slides and highlighting laboratory-scale effects. These key parameters were then normalized with Re, quantifying the degree to which these scale effects can be correlated to air-related interactions. For the deposit runout distance, the normalization also included the data set from Davies et al. (1999) and natural events, to evaluate whether the relative importance of Re changes as the scale range increases further. This results in new scaling laws allowing laboratory results, under idealized conditions, to be quantitatively compared to natural slides by excluding Re scale effects, with equation (10) facilitating direct upscaling.

The laboratory setup, methodology, and the DEM approach are described in sections 2 and 3, while section 4 highlights laboratory-scale effects and key results from the DEM. Section 5 evaluates the dependence of these scale effects on Re. The most relevant conclusions are summarized in section 6.

2. Laboratory Setup and Methodology

A laboratory setup was designed to produce Fr-similar granular slides at three different scales. The scale factor λ, the ratio between a characteristic length at largest scale and at the chosen comparison scale, varies across a range of 1 to 4. The key parameters and scaling relating to the ramp geometry and slides across the experimental range are defined in Figure 1 and Table 1. Images of the laboratory setups at $\lambda = 1$, 2, and 4 are provided in the supporting information (Figure S1); all configurations had the same layout in terms of measurement equipment, chute geometry, and moving parts. The channel was frictional but smooth, with smooth channels being relevant to industrial contexts and providing a useful simplification and foundation for evaluating scale effects caused by other factors in dry granular slides.

The x coordinate denotes the position downward parallel to the channel surface, with x_f, x_m, x_c, and x_t representing the respective channel-wise slide front, peak, mass centroid, and tail positions. The y coordinate denotes the perpendicular distance from the left-hand sidewall in Figure 1b with w representing the channel width. The z coordinate denotes the position perpendicular to the channel surface, with h_m being the maximum slide thickness at the channel centerline ($y = 0$). d is the mean particle diameter and ω_{sh} is the constant rate of shutter angular acceleration after release, resulting in a velocity u_{sh} at the shutter tip after rotating 90°. H_s and L_s describe the slide release wedge shape, resulting in an angle θ_W between the wedge surface and the flat runout zone. H_c represents the initial height of the slide mass centroid above the flat runout zone. M_s and V_s indicate the slide mass and volume. L_1 denotes the distance from the release point
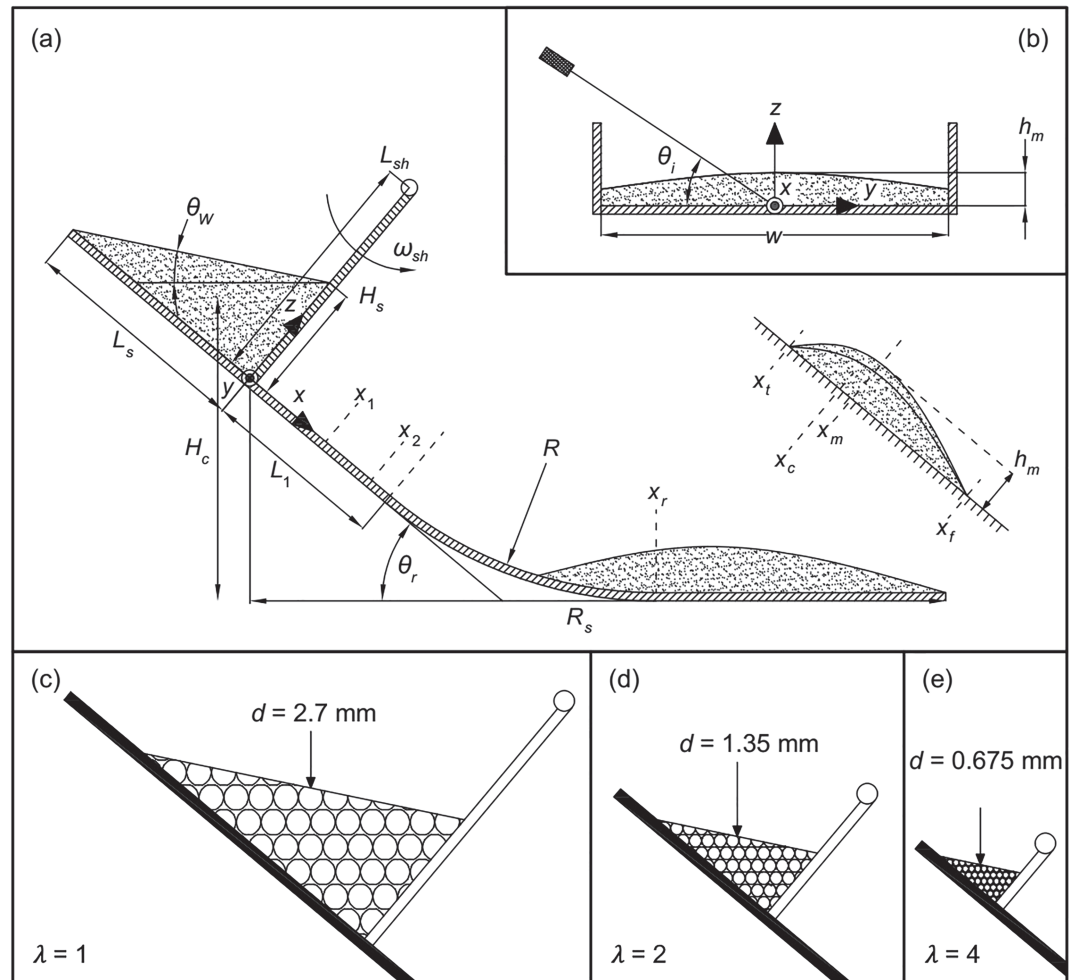
Figure 1. Key parameters and Fr scale series of granular slides. (a) Channel side view, with x, y, z denoting the curvilinear position coordinate system. (b) Slide cross section across channel width. (c–e) Relative scaling of release wedges, channel, and mean particle diameter d varying with scale factor λ.

to the onset of the curved transition zone, of radius R, and L_{sh} denotes the distance between the shutter rotation axis and the channel surface. x_1 and x_2 describe the positions of specific measurement zones from the release point, at which high-speed camera and laser trigonometry measurements (with incidence angle θ_i) were made. θ_r is the channel inclination angle, x_r represents the position at which the transition curve ends and R_s is the final front distance from x_r, while f is the image frame rate.

w was 0.250, 0.500, or 1.000 m, while L_1 was 0.578, 1.155, or 2.310 m, depending on λ. θ_r was fixed at 40°, well above the friction angle of the slide material to ensure a steady avalanche from release to deposit. High-speed cameras were positioned perpendicular to the inclined channel surface to measure the surface velocity u_s via particle image velocimetry, while the surface thickness was calculated using the shift in a laser point visible in the camera images. u_s acts primarily in the x direction, making it nearly identical to u_x, the ramp-wise slide velocity. The slide runout distances and deposit morphologies were measured via photogrammetry (Kesseler, 2019; Kesseler et al., 2018).

Garside Sands aggregates were used with particle diameters varying between 0.5 and 1.0 mm at $\lambda = 4$, between 1.0 and 2.0 mm at $\lambda = 2$, and between 2.0 and 4.0 mm at $\lambda = 1$ (Table 1), with similar angularity and size distribution curves at all scales. d is d_{50} for the laboratory particles, representing the sieve size with 50% average passing and corresponding well to the volume-based particle size. d was preferred to other characteristic diameters such as the Sauter mean diameter (which Kowalczuk and Drzymala (2016) suggest may be relevant) due to its ease of application and relevance for both drag and collisional/contact contexts. The material stiffness was constant between scales.

Table 1
Key Laboratory and Numerical Parameters, Satisfying Froude Scaling Laws

Exp.	Exp. type	λ	d	L_1	R	L_{sh}	ω_{sh}	u_{sh}	w	θ_W	L_s	H_s	x_1	x_2	x_r	V_s	M_s	f
(-)	(-)	(-)	(mm)	(m)	(m)	(m)	(rad/s^2)	(m/s)	(m)	(°)	(m)	(m)	(m)	(m)	(m)	(m^3)	(kg)	(Hz)
L1–L6	Laboratory	1	2.7	2.310	0.246	0.500	19.6	1.93	1.00	0	0.298	0.250	0.800	1.600	2.490	3.7×10^{-2}	60.30	1,000
L7–L12	Laboratory	1	2.7	2.310	0.246	0.500	19.6	1.93	1.00	7.5	0.392	0.250	0.800	1.600	2.490	4.9×10^{-2}	79.42	1,000
L13–L17	Laboratory	1	2.7	2.310	0.246	0.500	19.6	1.93	1.00	15.0	0.536	0.250	0.800	1.600	2.490	6.7×10^{-2}	108.51	1,000
L18–L21	Laboratory	2	1.35	1.155	0.123	0.250	39.2	1.37	0.50	0	0.149	0.125	0.400	0.800	1.245	4.7×10^{-3}	7.54	1,414
L22–L25	Laboratory	2	1.35	1.155	0.123	0.250	39.2	1.37	0.50	7.5	0.196	0.125	0.400	0.800	1.245	6.1×10^{-3}	9.93	1,414
L26–L29	Laboratory	2	1.35	1.155	0.123	0.250	39.2	1.37	0.50	15.0	0.268	0.125	0.400	0.800	1.245	8.4×10^{-3}	13.56	1,414
L30–L37	Laboratory	4	0.675	0.578	0.062	0.125	78.5	0.97	0.25	0	0.074	0.063	0.200	0.400	0.622	5.8×10^{-4}	0.94	2,000
L38–L45	Laboratory	4	0.675	0.578	0.062	0.125	78.5	0.97	0.25	7.5	0.098	0.063	0.200	0.400	0.622	7.7×10^{-4}	1.24	2,000
L46–L53	Laboratory	4	0.675	0.578	0.062	0.125	78.5	0.97	0.25	15.0	0.134	0.063	0.200	0.400	0.622	1.0×10^{-3}	1.70	2,000
S1	Simulation	1	2.7	2.310	0.246	0.500	19.6	1.93	1.00	0	0.298	0.250	0.800	1.600	2.490	3.7×10^{-2}	56.25	1,000
S2	Simulation	1	2.7	2.310	0.246	0.500	19.6	1.93	1.00	7.5	0.392	0.250	0.800	1.600	2.490	4.9×10^{-2}	74.16	1,000
S3	Simulation	1	2.7	2.310	0.246	0.500	19.6	1.93	1.00	15.0	0.536	0.250	0.800	1.600	2.490	6.7×10^{-2}	101.29	1,000
S4	Simulation	2	1.35	1.155	0.123	0.250	39.2	1.37	0.50	0	0.149	0.125	0.400	0.800	1.245	4.7×10^{-3}	6.99	1,414
S5	Simulation	2	1.35	1.155	0.123	0.250	39.2	1.37	0.50	7.5	0.196	0.125	0.400	0.800	1.245	6.1×10^{-3}	9.27	1,414
S6	Simulation	2	1.35	1.155	0.123	0.250	39.2	1.37	0.50	15.0	0.268	0.125	0.400	0.800	1.245	8.4×10^{-3}	12.63	1,414
S7	Simulation	4	0.675	0.578	0.062	0.125	78.5	0.97	0.25	0	0.074	0.063	0.200	0.400	0.622	5.8×10^{-4}	0.88	2,000
S8	Simulation	4	0.675	0.578	0.062	0.125	78.5	0.97	0.25	7.5	0.098	0.063	0.200	0.400	0.622	7.7×10^{-4}	1.16	2,000
S9	Simulation	4	0.675	0.578	0.062	0.125	78.5	0.97	0.25	15.0	0.134	0.063	0.200	0.400	0.622	1.0×10^{-3}	1.58	2,000
S10	Simulation	0.2	13.5	11.55	1.232	2.500	3.92	4.33	5.00	0	1.490	1.250	4.000	8.000	12.448	4.655	6,985.1	447
S11	Simulation	20	0.135	0.116	0.012	0.025	392.0	0.43	0.05	0	0.015	0.013	0.040	0.080	0.124	7.0×10^{-6}	7.4×10^{-3}	4,472

Note. Constant parameters across all experiments: channel inclination angle $\theta_r = 40°$, internal friction angle $\phi = 30°$, ramp bed friction angle $\delta_i = 30°$, runout bed friction angle $\delta_r = 28.5°$, grain density $\rho_g = 2{,}650$ kg/m^3, restitution coefficient $e = 0.893$, grain Young's modulus $E = 65$ GPa, and steel Young's modulus $= 210$ GPa.

Table 2
Initial (Fr_i, Re_i, Ca_i) and Measured (Fr, Re, Ca) Force Ratios

Experiment no.	λ	H_c	u_i	h_i	Fr_i	Re_i	Ca_i	u_s	h_m	Fr	Re	Ca
(-)	(-)	(m)	(m/s)	(m)	(-)	(-)	(-)	(m/s)	(m)	(-)	(-)	(-)
L1–L6	1	1.664	3.19	0.0161	8.02	570	3.86×10^{-7}	3.15	0.0149	8.24	563	3.76×10^{-7}
L7–L12	1	1.684	3.21	0.0212	7.03	574	3.90×10^{-7}	3.19	0.0155	8.18	570	3.85×10^{-7}
L13–L17	1	1.716	3.24	0.0290	6.07	579	3.98×10^{-7}	3.24	0.0162	8.13	579	3.97×10^{-7}
L18–L21	2	0.832	2.26	0.0081	8.02	202	1.93×10^{-7}	2.06	0.0088	7.01	184	1.61×10^{-7}
L22–L25	2	0.842	2.27	0.0106	7.03	203	1.95×10^{-7}	2.11	0.0094	6.95	189	1.69×10^{-7}
L26–L29	2	0.858	2.29	0.0145	6.07	205	1.99×10^{-7}	2.15	0.0101	6.83	192	1.75×10^{-7}
L30–L37	4	0.416	1.60	0.0040	8.02	71	9.64×10^{-8}	1.39	0.0052	6.15	62	7.31×10^{-8}
L38–L45	4	0.421	1.61	0.0053	7.03	72	9.75×10^{-8}	1.40	0.0059	5.82	63	7.42×10^{-8}
L46–L53	4	0.429	1.62	0.0073	6.07	72	9.94×10^{-8}	1.42	0.0066	5.58	63	7.63×10^{-8}

A Froude scaling approach was used, with lengths scaling linearly with λ, velocities and time scaling with $\lambda^{1/2}$, and mass scaling with λ^3. In this study, $Fr = u/\sqrt{gh}$, with u being the slide velocity and h being the slide thickness. Initial estimates of relevant Fr, Re, and Ca have been calculated to clarify the scaling approach. For Fr_i, an initial characteristic velocity u_i is derived from the energy balance of a frictional block sliding down a slope (Körner, 1977), resulting in

$$u_i = \sqrt{2gH_c(1 - \tan\delta_i/\tan\theta_r)}, \tag{4}$$

with H_c denoting the vertical distance of the mass centroid of the release wedge from the runout zone. An initial characteristic length h_i is derived from the mean thickness of the slide spread evenly along the inclined channel length from the shutter to the transition curve, resulting in

$$h_i = \frac{H_s^2 \tan(90 - \theta_r + \theta_W)}{2L_1}. \tag{5}$$

The resulting Fr_i, Re_i, and Ca_i are thus defined as

$$Fr_i = \frac{u_i}{\sqrt{gh_i}} = \frac{2}{H_s}\sqrt{\frac{H_c L_1(1 - \tan\delta_i/\tan\theta_r)}{\tan(90 - \theta_r + \theta_W)}}, \tag{6}$$

$$Re_i = \frac{u_i d}{\nu_f} = \frac{d}{\nu_f}\sqrt{2gH_c(1 - \tan\delta_i/\tan\theta_r)}, \tag{7}$$

$$Ca_i = \frac{\rho_g u_i^2}{E} = \frac{2\rho_g g H_c(1 - \tan\delta_i/\tan\theta_r)}{E}, \tag{8}$$

with ν_f being $1.5 \times 10^5 \, \text{m}^2/\text{s}$ at room temperature. The initially calculated (Re_i and Ca_i) and measured (Re and Ca) values of force ratios differ greatly across the laboratory-scale series (Table 2), confirming that experiments scaled to have identical Fr display large differences in Re and Ca, responsible for scale effects. While it is difficult to compare granular slides effectively with a single representative value of Fr (Ng et al., 2019), this comparison is useful for validating the presence of scale effects in the present study.

Multiple experiments have been conducted for each initial condition at each scale (Table 1) to generate ensemble-averaged slide data. This reduced the measurement uncertainty of these parameters by a factor of $\sqrt{N}$, where N is the number of experimental repeats. $N = 4$ for laboratory experiments with $\lambda = 2$, $N = 5$ for $\lambda = 1$ and $\theta_W = 15°$, $N = 6$ for other θ_W with $\lambda = 1$, and $N = 7$ for $\lambda = 4$.

Deposit front and tail positions measured with a digital camera involved a timing uncertainty of $\pm0.017 \, \text{s}$ due to $f = 30 \, \text{Hz}$, and a positioning uncertainty of $\pm0.01 \, \text{m}$ due to the camera resolution. The uncertainty in the particle image velocimetry velocity vectors at specific time steps is estimated as $\pm2.5\%$, with timing uncertainty of ±1 camera frame at each scale (Table 1). Slide thickness measurements were influenced by uncertainty in the ramp coordinates in the camera footage ($\pm2.5\%$), uncertainty caused by stray particle interference with the lasers ($\pm10\%$), and uncertainty in θ_i ($\pm5\%$), compounding to a total thickness uncertainty of $\pm11.2\%$. Deposit position uncertainty in the photogrammetric meshes is $\pm0.5 \, \text{mm}$ for all λ.

Table 3
Key DEM Parameters

Experiment no.	λ	n	T_s	T_r	Δt_c	Δt_s
(-)	(-)	(-)	(s)	(s)	(s)	(s)
S1	1	1.95×10^6	0.130	2.958	6.12×10^{-7}	3.54×10^{-7}
S2	1	2.56×10^6	0.140	3.040	6.12×10^{-7}	3.54×10^{-7}
S3	1	3.51×10^6	0.140	3.112	6.12×10^{-7}	3.54×10^{-7}
S4	2	1.94×10^6	0.085	2.107	3.06×10^{-7}	1.77×10^{-7}
S5	2	2.56×10^6	0.092	2.171	3.06×10^{-7}	1.77×10^{-7}
S6	2	3.49×10^6	0.099	2.205	3.06×10^{-7}	1.77×10^{-7}
S7	4	1.94×10^6	0.065	1.473	1.53×10^{-7}	8.84×10^{-8}
S8	4	2.56×10^6	0.065	1.518	1.53×10^{-7}	8.84×10^{-8}
S9	4	3.49×10^6	0.070	1.552	1.53×10^{-7}	8.84×10^{-8}
S10	0.2	1.95×10^6	0.269	6.619	3.06×10^{-6}	1.77×10^{-6}
S11	20	1.94×10^6	0.027	0.660	3.06×10^{-8}	1.77×10^{-8}

3. DEM Modeling

This study involves DEM simulations based on the Large-scale atomic/molecular massively parallel simulator Improved for General Granular and Granular Heat Transfer Simulations (LIGGGHTS) engine of Kloss et al. (2012). LIGGGHTS models particle contacts via a linear spring-dashpot model with Lagrangian trajectory calculation. Normal and tangential contact forces are calculated using properties including the Poisson ratio, friction coefficients, restitution coefficient, shear modulus, and Young's modulus, using a nonlinear Hertz (1882) contact model (Kloss et al., 2012). Details for the DEM settings used in this study are given in Kesseler et al. (2018) and Kesseler (2019).

A rolling-resistance method has been adapted to simulate the shape effects of the spherical particles of the DEM. The sphericity and angularity of the laboratory sand particles were modeled through the application of rolling friction torques during particle-particle and particle-surface collisions (Ai et al., 2011; Wensrich & Katterfeld, 2012). The coefficient of rolling resistance μ_r is physically derived from the mean eccentricity of contacts from the mass centroid of a particle and can be derived from the angle at which the gravity and rolling-resistance torques acting on a particle are balanced (Ai et al., 2011).

The distance threshold for the detection of particle collisions was set to $2d$ in this study. The particle size distribution was represented via Gaussian distributions with mean volume-based d and standard deviations of d closely matching the laboratory particles at their respective scales (i.e., a mean of 2.7 mm and a standard deviation of 0.4 mm at $\lambda = 1$). The DEM particles were gravity deposited to ensure that the release wedge structure was modeled with sufficient accuracy.

The simulation time step Δt_s was determined for each experimental scale, using the Rayleigh wave speed to determine a critical threshold for adequate calculation stability. The resulting critical time step Δt_c (Thornton, 2015) is proportional to d, meaning that smaller simulations require more time steps to simulate the same duration after Froude scaling. The simulation time steps were set to less than 60% of Δt_c at each scale; this value was deemed sufficient to prevent calculation instability entirely. Δt_c, the final time step Δt_s, the particle count n, the settlement time T_s, and the respective runout completion time T_r for all simulations are shown in Table 3.

The LIGGGHTS code has been calibrated and validated with an own column collapse experiment (Figure S2) and a granular chute slide experiment from Hutter et al. (1995) (Figure S3). μ_r was set to 0.28, while the rolling viscous damping ratio η_r was set to 0.30, and the restitution coefficient e to 0.893.

4. Laboratory Scale Effects in the Scale Series

This section contains key data from the scale series. While experiments were conducted for $\theta_W = 0°$, 7.5°, and 15°, only the results for $\theta_W = 0°$ are presented here with the remaining results provided in the supporting information. The total data set comprises nine different laboratory slide geometries (Table 1). Overall, the laboratory data shows significant scale effects across many of the key parameters, such as slide
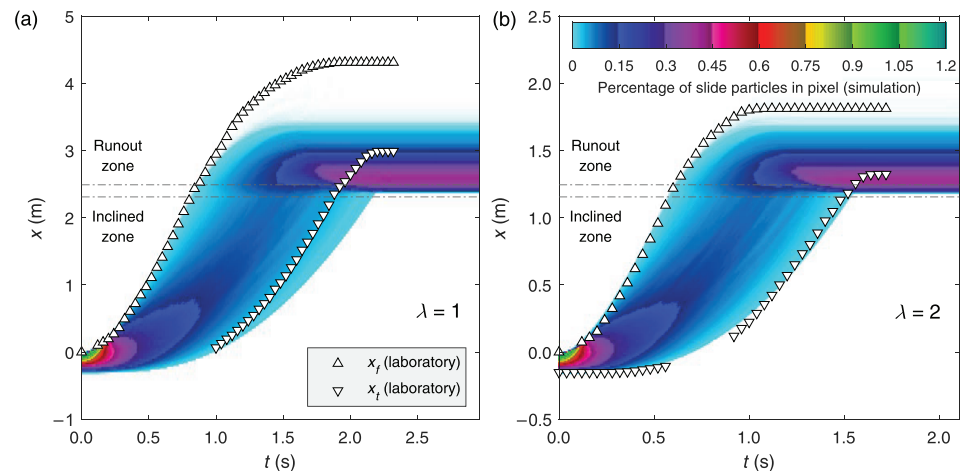
Figure 2. Comparison of position distribution along the channel center x over time t between (a) laboratory (L1–L6) and simulation (S1) slides for $\lambda = 1$ and $\theta_W = 0°$ and (b) laboratory (L18–L21) and simulation (S4) slides for $\lambda = 2$ and $\theta_W = 0°$.

position distribution over time, deposition patterns, and the slide surface velocity, with other parameters such as the slide thickness also being influenced by these scale effects indirectly.

A comparison of the ensemble-averaged laboratory position distributions at the channel centers for $\lambda = 1$ and 2 and $\theta_W = 0°$, together with the simulation data for $\lambda = 2$ shown in Figure 2, reveals large differences between scales. The laboratory fronts and tails in Figure 2a ran out 26% further on average than predicted by the DEM. The DEM accurately matches the front and tail positions of the laboratory experiments at $\lambda = 2$ until the slides start to settle. Despite the DEM showing little evidence of scale effects, the laboratory data quickly diverges from the DEM data as the slides start to decelerate. The tails show a strong mismatch at $\lambda = 1$ long before reaching the transition curve with the laboratory slide tails depositing beyond the transition curve, in contrast to the tails at $\lambda = 2$. However, at $\lambda = 1$, the laboratory slide fronts still match the simulation data well until they pass over the transition curve. Overall, while the DEM reproduced most features at $\lambda = 2$, a mismatch is seen at $\lambda = 1$ due to the DEM excluding air responsible for Re scale effects.

Similar slide position data for the channel sidewall region can be seen in Figure S4, with Figures S5 to S8 providing the corresponding data for other values of θ_W. The discrete fronts of the simulated slides occur where the cyan in the color map is strongest, with the dispersed front region being represented by fainter shades tending toward white. These dispersed fronts and tails are also visible during the laboratory experiments (Figures S9 and S10), with the fronts behaving similarly to those in the DEM but displaying more dispersion due to individual particle angularity. However, the simulated tails deposited in the transition curve and lagged behind the laboratory tails throughout, particularly at the sidewalls (Figure S7), resulting in stronger tail curvature. Some laboratory tail data was missing due to the shutter blocking the visual access for the digital camera, but the trends of the laboratory tail position remain clear throughout.

The surface velocity magnitude and behavior are also subject to significant scale effects in the laboratory experiments. The differences in the dimensional simulation data in Figure 3a mostly disappear in the nondimensionalization seen in Figure 3b. However, the differences in the corresponding laboratory data are not entirely eliminated in Figure 3b, displaying scale effects. The laboratory surface velocity data is represented as a moving average across a period of 25 camera frames (Table 1). The corresponding data for $\theta_W = 7.5°$ and 15° can be found in Figures S11 and S12, respectively. Generally, the front velocity quickly decelerates into a quasi-constant value as the bulk of the slide passes through the measurement point, before decelerating more rapidly again as the slide tail passes. Overall, the agreement between the laboratory and simulated $u_s/(gd)^{1/2}$ is reasonably good at $\lambda = 2$. The improved data fit at the same λ value compared to the position distributions in Figure 2 suggests that the simulated base velocity is reduced, resulting in increased shearing due to similar $u_s/(gd)^{1/2}$.

At $\lambda = 4$ the slides arrived at each measurement point slightly later than at lower λ values; this corresponds to $u_s/(gd)^{1/2}$ decreasing with reduced slide size. While the difference in $u_s/(gd)^{1/2}$ between $\lambda = 2$ and 4 is
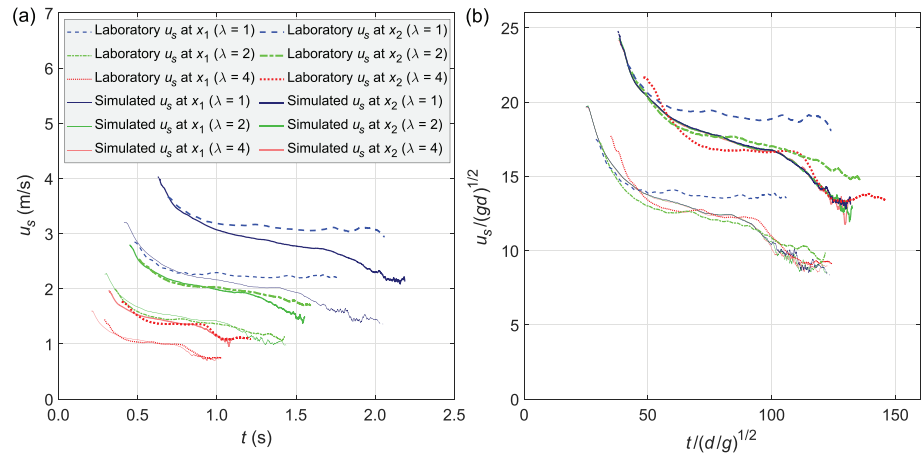
Figure 3. Comparison of the slide surface velocity profiles over time at x_1 and x_2 in (a) dimensional and (b) nondimensional form. Laboratory (L1–L6, L18–L21, and L30–L37) and simulated (S1, S4, and S7) velocity measurements with $\theta_W = 0°$.

minor at x_1, $u_s/(gd)^{1/2}$ at x_2 is 7.5% smaller at $\lambda = 4$ than at $\lambda = 2$, suggesting that some slide scale effects manifest between x_1 and x_2. $u_s/(gd)^{1/2}$ is similar for all scales as the slide front crosses the measurement points, but decreases much more slowly thereafter at $\lambda = 1$. Between $\lambda = 1$ and $\lambda = 4$, this results in a relative difference in $u_s/(gd)^{1/2}$ of 31% at x_1 and 35% at x_2, respectively, as the slide tails pass.

The slide thicknesses measured at the channel sidewall at x_1 and at the channel center at x_2 at $\theta_W = 0°$ vary significantly in dimensional form (Figures 4a and 4b), with the simulation data collapsing neatly with nondimensionalization and remaining differences in the laboratory data indicating scale effects (Figures 4c and 4d). The data for $\theta_W = 7.5°$ and 15° is provided in Figures S13 and S14, respectively. Scatter clouds show
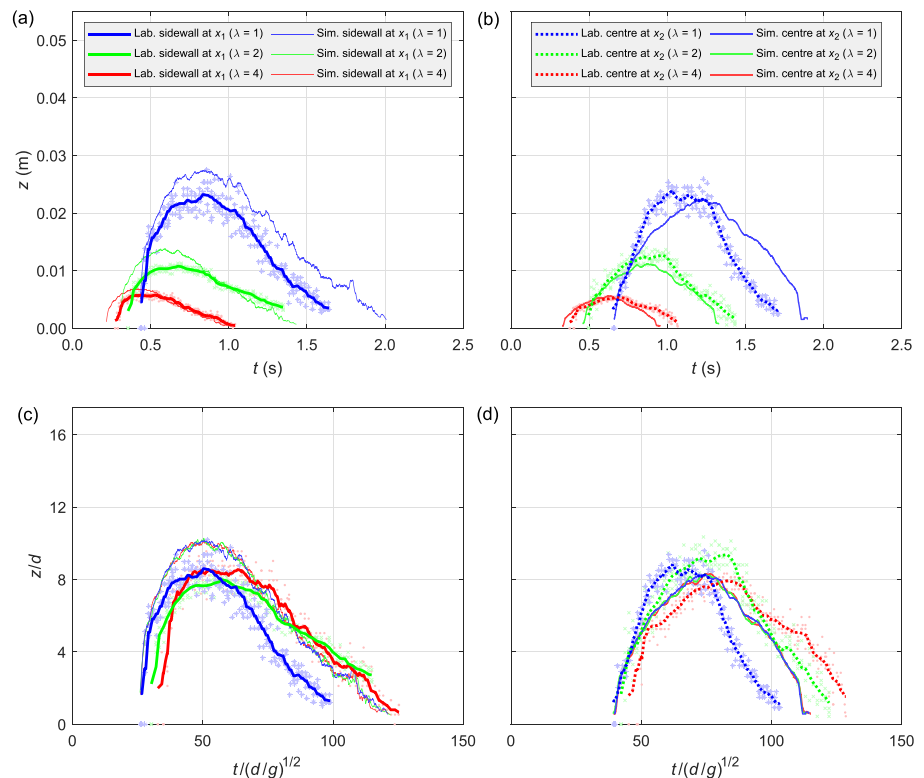

Figure 4. Comparison of laboratory and simulated slide thickness profiles over time for $\theta_W = 0°$ in (a, b) dimensional and (c, d) nondimensional form at (a, c) x_1 at the channel sidewall and (b, d) x_2 at the channel center.
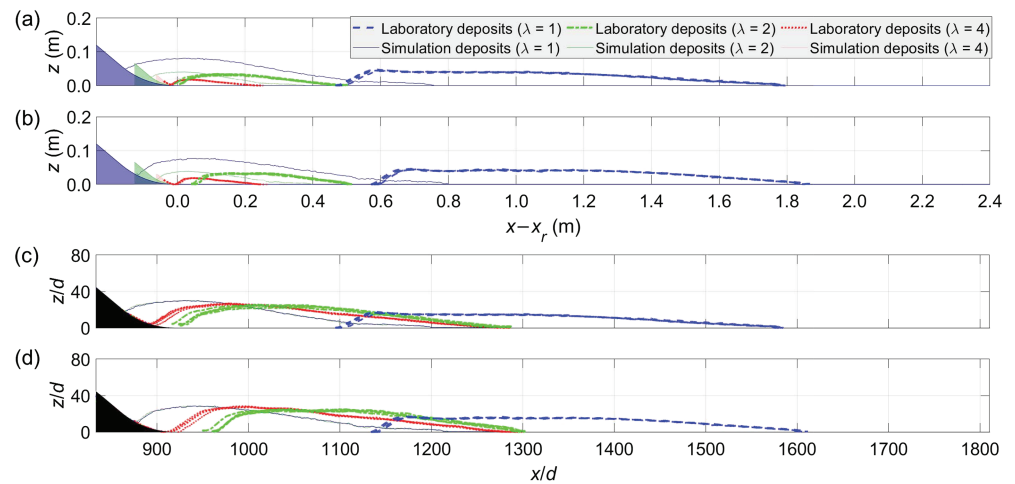
Figure 5. Comparison of laboratory and simulated (a, b) dimensional and (c, d) nondimensional deposit surfaces over distance for $\theta_W = 0°$ at (a, c) 10% across the channel width and (b, d) 50% across the channel width. The experimental numbers are shown in Table 1.

the variance within the discrete laboratory thickness measurements within each initial condition, which is due to the granularity of the slide surface and the occasional interference of loose particles. This variance relative to the mean peak slide thicknesses is $\pm 10\%$; after averaging, the variance of the laboratory thickness data is similar to that of the simulated data. The simulated slide thickness at $\lambda = 2$ is about 20% larger than in the laboratory at x_1. The agreement is much closer at x_2, demonstrating differences in shearing over the course of the slide event. The main scale effect at both x_1 and x_2 is the difference in thickness decrease after the peak is reached, with slides at larger sizes typically decreasing faster. This correlates with the increase in surface velocity previously seen in Figure 3. Furthermore, the duration at which the peak thickness is maintained increases as λ increases, showing that the peak is steeper at larger scales. The variation of the maximum slide thickness with λ is inconsistent, however.

After settling, the laboratory slide deposits are relatively flat and have cleared the transition curves, while the simulated tails deposit roughly halfway up the transition curve and the fronts run out over a shorter distance. The dimensional deposit surfaces with $\theta_W = 0°$ vary greatly across experimental scales (Figures 5a and 5b), with nondimensionalization collapsing the simulated deposits neatly but still revealing large-scale effects in the laboratory deposits (Figures 5c and 5d). Related data for $\theta_W = 7.5°$ and $15°$ is provided in Figures S15 and S16, respectively, with Tables S1 to S3 providing more detailed information on the deposit dimensions for $\theta_W = 0°$ to $15°$. For ease of comparison, the dimensional deposit surfaces in Figures 5a and 5b are presented in terms of $x - x_r$, denoting the distance from the end of the transition curve, while the nondimensional data in Figures 5c and 5d are presented with x (the distance from the shutter release) as defined in section 2. Data from individual laboratory experiments illustrates the high repeatability.

Significant changes can be seen in the nondimensional laboratory deposits as λ varies in Figures 5c and 5d. At $\lambda = 1$, the mean central tail position is $221d$ ahead of that at $\lambda = 4$ (a relative difference of 24%), while the mean central front position at $\lambda = 1$ is $333d$ ahead of that at $\lambda = 4$ (a relative difference of 26%). While the large-scale deposits are typically flat with little lateral curvature, the smaller laboratory deposits show a smoother curved surface with greater lateral curvature. This suggests that the influence of sidewall friction on the slide lateral shearing behavior is reduced at larger scales compared to other factors, potentially including air interactions. These scale differences were not seen in the corresponding numerical simulations, suggesting that the responsible physical mechanism is not captured by the DEM. Mechanisms present in the laboratory slides that are absent from the DEM and may facilitate scale effects are discussed in section 5.

While the scale effects captured by the laboratory experiments are not present in the simulation data, additional simulations conducted with λ values of 0.2 and 20 reveal some slight scale effects over this geometric scale difference of 100. The tail positions increased by up to $3d$ and the front positions by up to $18d$ as the size increased (Figure S17). These differences are Ca scale effects caused by constant material stiffness with

scale, and are derived from subtle changes in the slide velocity over time between these scales (Figures S18 and S19). These effects are very small in comparison to the total laboratory scale effects observed. They may have a minor impact on contact force transmission in physical models that would result in minor runout distance increases in scale series between much larger ranges of λ. However, this impact may not lead to the same outcomes with real angular particles and is insignificant compared to the main mechanism driving the laboratory scale effects.

5. Grain Reynolds Number Dependence

Overall, clear scale effects have been identified in the slide position distribution, the deposit shape and settlement behavior, and the slide surface velocity of the laboratory slides within a small scale range of $\lambda = 1$ to 4. While the simulation captured negligibly small scale effects within a larger scale range of $\lambda = 0.2$ to 20, the DEM failed to model the laboratory scale effects with the same Fr distributions being seen across the slide length at all moments in the slide events (Figure S20). This strongly suggests that the governing mechanism leading to scale effects is not modeled by the DEM. While the laboratory slides differ from the simulated slides due to particle angularity and contact-based effects that could indirectly lead to differences in slide dilation, contraction, and stress states (Kesseler et al., 2018), these are model effects and should not be responsible for the scale effects seen in the laboratory data. Additional key mechanisms that act exclusively on the laboratory slides include air, particle fracture, and subsequent dust generation.

While dust generation was insignificant at $\lambda = 4$ in the laboratory, the channel was coated in a very thin layer of dust at $\lambda = 1$ after each experiment (Figure S21), suggesting that dust generation increases with size. The degree to which this dust formation influences the energy balance of the slides during motion is an open question. However, measurements of the particle sphericity and angularity of sand grains before and after the experiments showed no significant changes, and the mass of dust generated per experiment was very low, perhaps within 0.01% of the slide mass. To further validate whether particle fracture was likely to be significant, we compared the highest mass-specific kinetic energy of particles at $\lambda = 1$ to the mass-specific fracture energy of similar quartz particles in Tavares and King (1998). Considering that only a small fraction (5-20%) of a particle's kinetic energy is lost in a collision event, we found the corresponding mass of dust generated to be in line with our previous estimate of 0.01%. As such, particle fracture was deemed unlikely to have created significant scale or model effects, but may become more relevant for $\lambda < 1$.

This leaves air fluidization and other Re-dependent phenomena as the primary mechanisms exclusive to the laboratory experiments responsible for scale effects. This hypothesis is supported by experimental evidence seen in the high-speed camera footage, such as the relative difference of front and tail dispersion observed in Figures S9 and S10 caused by more turbulent air structures. As the larger slides have more turbulent interactions with air due to higher Re, this turbulence may damp the dispersion caused by particle angularity more strongly at the larger scales. Additionally, increased randomness of individual particle motion was observed in the high-speed camera footage at the smaller scales, providing more physical evidence of air interactions. This section will analyze the degree to which Re is responsible for the observed scale effects, compared to other phenomena.

5.1. Normalization of the Slide Surface Velocity

To assess whether the surrounding air and turbulence are responsible for changes in slide behavior, the key parameters have been normalized with respect to Re, here defined with d_{50} and u_s. The nondimensional laboratory surface velocities from Figure 3 can be multiplied by a power α of Re at each moment in time as the slide passes through x_1 and x_2 (Figure 6a), with α being selected such that the experimental data at each scale collapses with maximized R^2 values. A complementary normalization has also been completed by using the estimated drag force on isolated surface particles to clarify the influence of this physical mechanism on observed scale effects (Figure 6b). The data for $\theta_W = 7.5°$ and 15° are shown in Figures S22 and S23, respectively.

The fit lines through the collapsed data in Figure 6 are polynomials that start when $t_* = 0$, which is the nondimensional time at which the slide front reaches the measurement point. These polynomials follow the structure

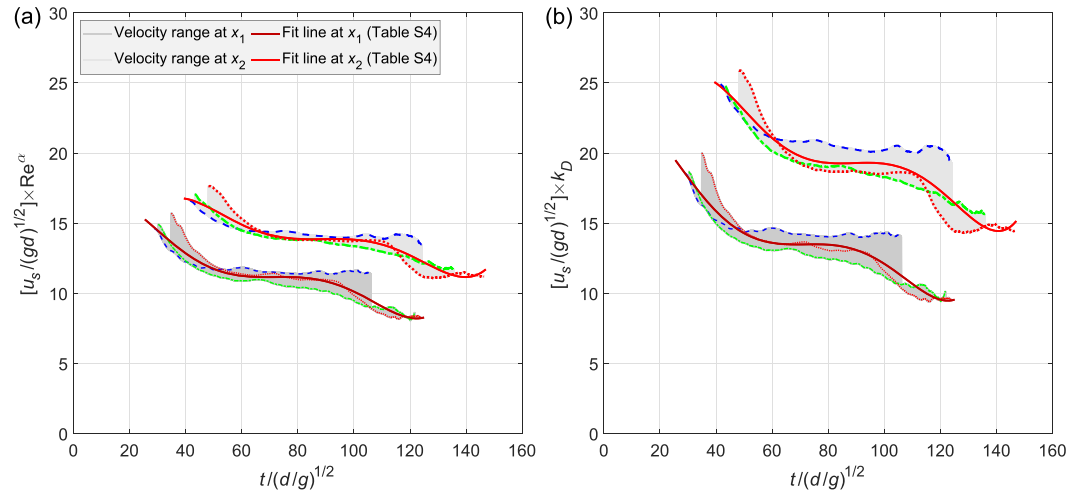$$t(d/g)^{1/2} = T_0 + T_1 t_* + T_2 t_*^2 + T_3 t_*^3 + T_4 t_*^4 + T_5 t_*^5. \tag{9}$$

Figure 6. Comparison of (a) Re-normalized and (b) k_D-normalized nondimensional slide surface velocity $u_s/(gd)^{1/2}$ profiles over nondimensional time $t/(d/g)^{1/2}$ with $\theta_W = 0°$. Dotted data lines correspond to the respective data in Figure 3b.

The structure of equation (9) allows the main features of the velocity profiles to be captured, such as the sharp decrease in initial velocity leveling out as the bulk of the slide passes. For example, T_4 and T_5 mostly relate to the fit toward the passing of the slide tails. The coefficients T_0 to T_5 of the original and normalized data in Figures 3 and 6 are displayed in Table S4 (see Tables S5 and S6 for $\theta_W = 7.5°$ and $15°$, respectively).

As the particles accelerate under gravity, Re increases, impacting the instantaneous drag coefficient C_D and causing the terminal velocity to evolve over time (Kesseler, 2019). A drag force normalization factor k_D can be applied based on Re and the particle shape-dependent C_D (Bagheri & Bonadonna, 2016), representing the ratio of the drag-free (u_f) and drag-influenced (u_d) instantaneous velocity as it varies from release to terminal velocity. The drag-influenced laboratory surface velocity can then be multiplied by the appropriate k_D to estimate a "drag-free" velocity (Figure 6b). C_D and k_D vary significantly between scales due to differences in
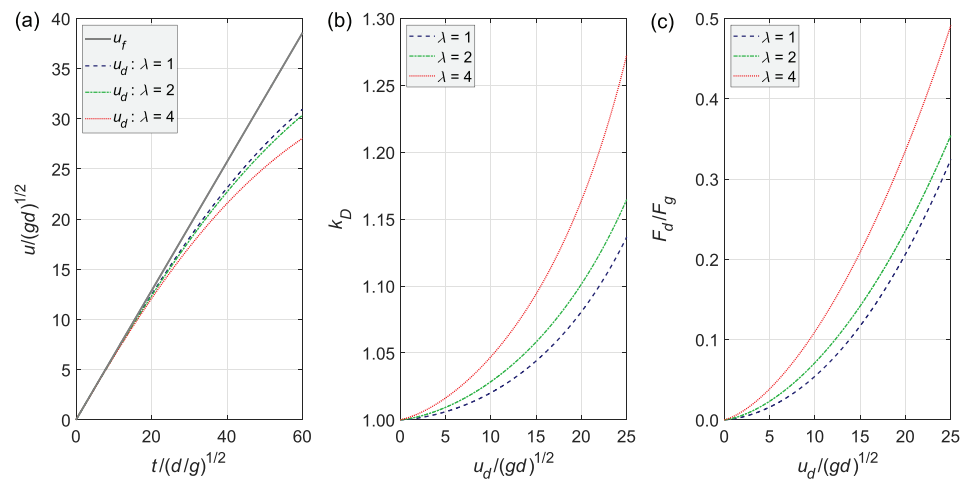

Figure 7. Model for the calibration of u_s to remove the influence of particle drag force F_d for $\lambda = 1$ to 4. (a) Evolution of nondimensional particle drag-free velocity $u_f/(gd)^{1/2}$ and nondimensional particle drag-influenced velocity $u_d/(gd)^{1/2}$ over nondimensional time $t/(d/g)^{1/2}$. (b) Evolution of drag force normalization factor k_D over nondimensional particle drag-influenced velocity $u_d/(gd)^{1/2}$. (c) Evolution of particle drag/gravity force ratio F_d/F_g over nondimensional particle drag-influenced velocity $u_d/(gd)^{1/2}$.

Re. The evolution of u_f, u_d, k_D, and the ratio of the grain drag force F_d and the grain gravity force F_g in this physically based model is highlighted in Figure 7.

Within experimental ranges of velocity, F_d at x_1 can reach 17% of F_g at $\lambda = 1$, and up to 28% at $\lambda = 4$. Meanwhile, F_d at x_2 can reach 32% of F_g at $\lambda = 1$, and up to 50% at $\lambda = 4$, with even stronger influence closer to the transition curve. These correspond to respective k_D values of 1.07, 1.13, 1.15 and 1.30. By calibrating the laboratory data to isolate and remove the impact of the estimated drag force on the slide surface velocity, the fit improvement shows to which degree the particle drag force is responsible for the Re scale effects seen in Figure 6a. The related data for $\theta_W = 7.5°$ and $15°$ are shown in Figures S22b and S23b, respectively.

Generally, an improvement of the data fit with the Re normalization is observed at both x_1 and x_2. The R^2 values of the original data (Figure 3b) increased from 0.820 and 0.759 at x_1 and x_2, respectively, to 0.847 and 0.865 with Re^α normalization, and to 0.828 and 0.818 with k_D normalization. $\alpha = -0.029$ was selected at x_1 and $\alpha = -0.047$ at x_2. A smaller degree of fit improvement is observed with the k_D-normalization, reaching 30% of the Re normalization fit improvement at x_1 and 55% at x_2, respectively. The fit improvement of the surface velocity between scales reaches about 15% at x_1 and about 44% at x_2. This collapse is typically best during the middle phase of the slide, apart from the initial timing differences of the front arrival and differences in the final tail velocities. The value of α selected for the best fit increases from x_1 to x_2, suggesting that the surface velocity is more Re-dependent further down the ramp and scale effects accumulate with distance. A smaller but still consistent collapse of the surface velocities can be seen in Figure 6b, showing that much of the Re-dependence of scale effects is caused by the drag force acting on particles. The relative fit improvement is best at x_2 where particles move closer to the terminal velocity and the drag force becomes more dominant.

Overall, as the particle drag force correction approach does not capture all of the observed scale effects (Figure 6b), this suggests that other factors also contribute to Re scale effects, particularly at lower particle velocities. The interactions of air on the macroscale granular system may exert a particularly strong influence; differences in particle drag caused by changes in slide velocity may affect granular temperature and thus energy dissipation. This highlights the wide range of physical mechanisms that can influence Re scale effects.

5.2. Normalization of Slide Deposit Parameters

The front, peak, mass centroid, and tail runout distances of the laboratory slides with $\theta_W = 0°$ were also multiplied by Re^α, with α being the power selected to collapse the data with minimal error (RMSE = 0 corresponds to perfect agreement) (Figure 8). R_s denotes the ensemble-averaged horizontal distance between a specific position on the flat runout zone and the shutter release point.

As the slide deposits were stationary, Re at 100 frames (Table 1) after the front contacted the x_2 measurement point were used for reference, with $Re = 655.1$ at $\lambda = 1$, $Re = 226.6$ at $\lambda = 2$, and $Re = 78.7$ at $\lambda = 4$. For data for $\theta_W = 7.5°$ and $15°$ see Figures S24 and S25. The laboratory data converges toward single values after Re normalization, with fit improvement of 88% for x_f, 98% for x_m, 89% for x_c, and 93% for x_t. The degree of Re dependence observed in Figure 8 is much greater than that observed for the surface velocity (Figure 6a), and the deposit peak and tail positions were normalized more effectively than the deposit front and mass centroid positions. Overall, the high degree of fit improvement shows that scale effects are largely responsible for the observed changes in the deposit morphology. Re scale effects may impose second-order influences on the stress distribution through the slide particle contact network in ways that are not accounted for by Re on individual particles, which may be responsible for the remaining fit improvement.

As the slide front position (i.e., total runout) is the most relevant parameter for hazard assessment, further analysis was conducted with the volume-normalized total runout $R_s/V_s^{1/3}$ being compared with the volume-normalized fall height $H_c/V_s^{1/3}$ (Figure 9). The runout was then normalized again with respect to a relevant Re^α, to collapse the data. This comparison includes the laboratory experiments conducted in this study, as well as experiments of Davies et al. (1999), who investigated the relationship between H_c and R_s for a range of slide sizes and dimensions. While those experiments did not follow a Froude number scale series (for example, the slide release positions were not scaled with the slide volumes), they provide a large range of slide geometries for which the slide Re dependency can be evaluated, with inclination angles close to that of the present study.
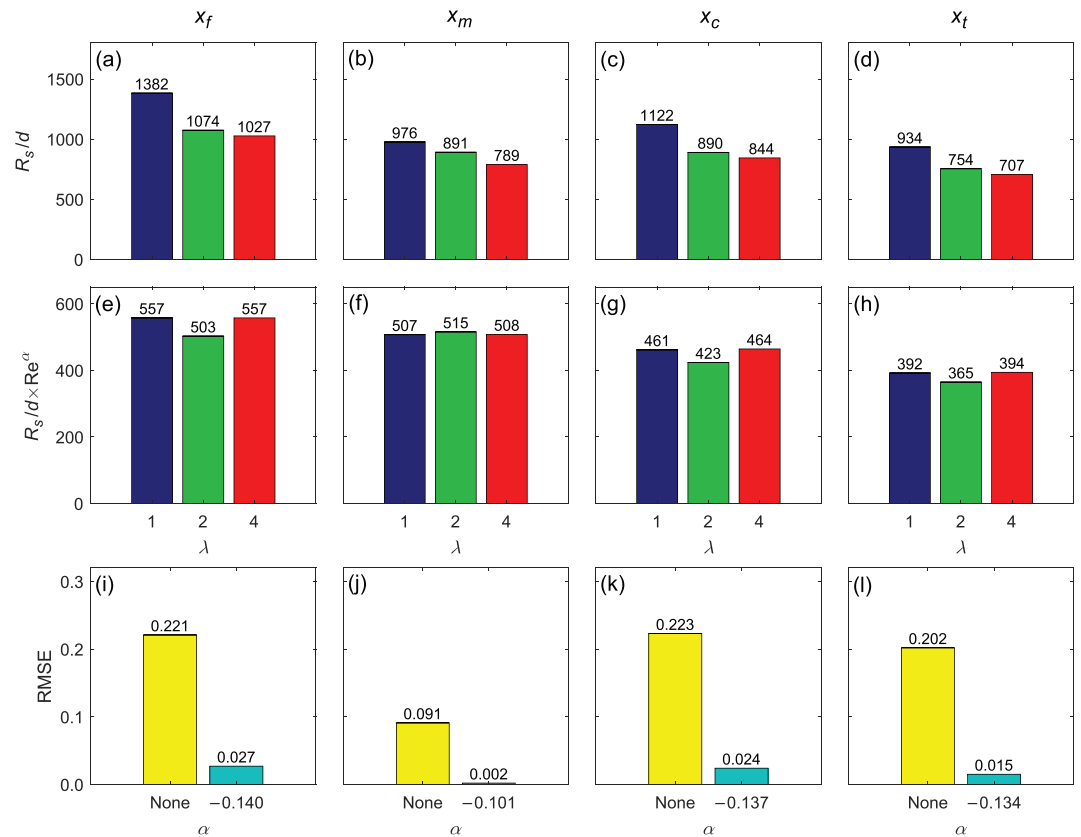
Figure 8. Re dependency of key laboratory deposit parameters for $\theta_W = 0°$. (a–d) Original position data, (e–h) Re-normalized data, and (i–l) prenormalization and postnormalization RMSE for (a, e, i) x_f, (b, f, j) x_m, (c, g, k) x_c, and (d, h, l) x_t.

The front velocities of these slides were estimated via conservation of energy, using equation (4), with $\delta_i = 29°$ and $\theta_r = 35°$ and $45°$ (Figure 9). This velocity, together with d_{50}, was then used to determine Re. The natural slide events included in this comparison consist of avalanches, rockfalls, and debris flows that displayed similar conditions to these laboratory experiments such as channelized sliding, relatively low moisture content, and insignificant entrainment, and had appropriate physical dimensions (Table S7). The fit line in Figure 9 is given by

$$H_c/V_s^{1/3} = 5.0 \ln\{\cosh[0.27(R_s/V_s^{1/3}) \times Re^\alpha]\}. \tag{10}$$

Notably, the laboratory experiments of the present study fall in line with those of Davies et al. (1999) for $\alpha = -0.091$, for which the majority of the natural slides also align. The unnormalized fit (not shown) improves by 61% with this Re normalization. By using equation (10), laboratory data can be upscaled to natural events under idealized conditions. This was not possible up to now (Iverson, 2015) and expands the purpose and utility of laboratory experiments for improving hazard prediction and mitigation capabilities.

The value $\alpha = -0.091$ is lower than those for the laboratory experiments alone (Figure 8), suggesting that other physical factors start to become relevant compared to Re-dependent fluidization at geophysical scales, corresponding to size effects rather than scale effects. These may include secondary mechanisms such as acoustic fluidization, frictional melting, and fragmentation (section 1). Some of the natural events in Figure 9 are outliers, with the Sherman Glacier[3], Rubble Creek[4], and Mount Cayley[8] slides still displaying increased runout distances after Re normalization. The Sherman Glacier slide[3] contained large amounts of snow and ice, which may have melted and fluidized during the slide event before resolidifying in the deposits analyzed in Shugar and Clague (2011). Additionally, the mean grain diameter d_{50} was selected as a characteristic particle diameter for the Re normalization, but smaller or larger grains may be more representative depending on the grain size distribution and other factors.
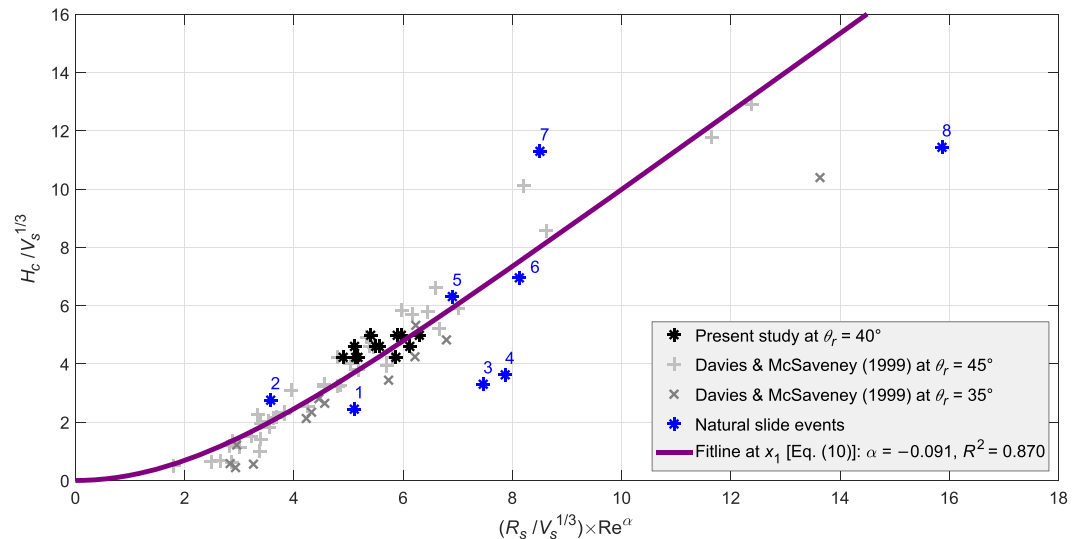
Figure 9. Fit of the normalized slide fall height $H_c/V_s^{1/3}$ and runout $\left(R_s/V_s^{1/3}\right) \times \mathrm{Re}^\alpha$ of laboratory experiments and natural slides with equation (10). Slide events: (1) Frank (1903) (Cruden & Hungr, 1986). (2) Elm (1881) (McKinnon, 2010). (3) Sherman Glacier (1964) (Shugar & Clague, 2011). (4) Rubble Creek (1855) (Moore, 1976). (5) Mount Cook (1991) (McSaveney, 2002). (6) Mount Steele (2007) (Lipovsky et al., 2008). (7) Thurweiser (2004) (Sosio et al., 2008). (8) Mount Cayley (1984) (Evans et al., 2001).

6. Conclusions

Scale effects make accurate modeling of large granular slides at reduced size in the laboratory difficult. A laboratory-numerical methodology to identify scale effects in granular slides has been developed under Froude number scaling laws. Geometrically similar laboratory experiments have been conducted between experiments with a size difference of 4, with slide masses ranging from 1 to 110 kg and grain Reynolds numbers (Re), defined with the mean grain diameter d_{50} and the surface velocity u_s, in the range of 10^2 to 10^3. DEM simulations have also been conducted to replicate the laboratory slide events, to allow the collection of additional data, to evaluate extrapolations of the scale series, and to verify whether the mechanisms causing laboratory scale effects manifest in the DEM.

Overall, the conducted laboratory experiments highlight clear differences with scale in dry granular slides. In particular, the surface velocity of slides increased by up to 35% as the scale increased. Generally, as the slides progressed down the channel, the laboratory surface velocities were highest and were very similar between scales, but as the slides continued the velocity decreased rapidly, particularly at the smallest scale. The tail velocity also decreased significantly at the smallest scale but did not at the largest scale. Experimental evidence such as changes in the dispersion of the slide fronts and tails in these regions suggests that air interactions are responsible for these differences. Additionally, the slide runout distance increased by up to 26% as the scale increased, as a result of the surface velocity differences seen. Properties such as the maximum slide thickness as it moved down the inclined channel section did not vary consistently with scale. The presence of these strong scale effects suggests that physical modelers should carefully calibrate their data to mitigate the influence of these scale effects before comparing it to natural events.

The DEM did not capture the significant scale effects identified in the laboratory scale series, highlighting that the physical factors causing these scale effects are not inherent to the physics of a granular system in absence of air. While some minor differences were observed between simulations of much greater and smaller sizes, these differences were insignificant within the laboratory range covered and are Cauchy number (Ca) effects caused by scale-invariant material stiffness. The low magnitude of these effects and lack of related physical behaviors in the laboratory experiments suggest that the influence of Ca on scale effects in dry granular slides is small.

A Re power law normalization, where key laboratory slide parameters such as surface velocity and runout distance are multiplied by a power α of Re, significantly improves the collapse of data from different scales. For example, the collapse of surface velocity is improved by up to 44% and the collapse of center-of-mass

runout distance is improved by up to 98% with this approach. This, in combination with experimental evidence from the laboratory experiments, suggests that Re strongly influences the scale effects identified in this study, with scale effects manifesting particularly strongly in the slide deposit positioning. Furthermore, calibration of the surface velocity with the particle drag force suggests that air-related mechanisms contribute to the Re scale effects, accounting for up to 55% of the Re^α-based fit improvement.

Comparisons of the laboratory results to slides from Davies et al. (1999) and natural events confirm the strong influence of Re scale effects. Finally, it has been demonstrated that laboratory-scale results can be effectively calibrated to model natural phenomena via Re normalization using equation (10) (Figure 9), expanding the utility of laboratory modeling for hazard prediction and mitigation.

Further DEM studies coupled with a computational fluid dynamics model could further support the influence of Re on scale effects in granular slides. Additional DEM studies using multisphere clumps with computational fluid dynamics coupling could further elucidate whether angularity inherently contributes to scale effects or whether it facilitates additional second-order Re scale effects.

Nomenclature

Ca	= Grain Cauchy number	(-)
Ca_i	= Initial grain Cauchy number	(-)
C_D	= Drag coefficient	(-)
d	= Mean grain diameter	(mm)
d_{50}	= 50th percentile grain diameter	(mm)
e	= Restitution coefficient	(-)
E	= Grain Young's modulus	(N/m^2)
f	= Image frame rate	(1/s)
F_d	= Grain drag force	(N)
F_g	= Grain gravity force	(N)
Fr	= Froude number	(-)
Fr_i	= Initial Froude number	(-)
g	= Gravitational acceleration	(m/s^2)
h	= Slide thickness	(m)
h_i	= Initial characteristic slide thickness	(m)
h_m	= Maximum slide thickness along centerline	(m)
H_c	= Height of slide mass centroid above runout area	(m)
H_s	= Initial slide thickness at shutter position	(m)
k_D	= Drag force normalization factor	(-)
L	= Characteristic length scale	(m)
L_s	= Initial slide length	(m)
L_{sh}	= Distance of axis of rotation from ramp surface	(m)
L_1	= Length of inclined ramp section	(m)
M_s	= Slide mass	(kg)
n	= Number of particles in simulation	(-)
N	= Number of experimental repeats	(-)
R	= Radius of ramp transition	(m)
R_s	= Slide horizontal runout distance from shutter release	(m)
R^2	= R squared value	(-)
Re	= Grain Reynolds number	(-)
Re_i	= Initial grain Reynolds number	(-)
RMSE	= Root mean square error	(-)
t	= Time	(s)
t_*	= Nondimensional time reference starting at 0 when slide reaches x_1 or x_2	(-)
T_r	= Slide runout completion time	(s)

T_s	= Settlement time	(s)
$T_0 - T_5$	= Polynomial fit coefficient	(-)
u	= Velocity	(m/s)
u_d	= Grain drag-influenced velocity	(m/s)
u_f	= Grain drag-free velocity	(m/s)
u_i	= Initial characteristic slide velocity	(m/s)
u_s	= Ramp-wise slide surface velocity	(m/s)
u_{sh}	= Shutter tip velocity	(m/s)
u_x	= Ramp-wise component of slide velocity	(m/s)
U	= Characteristic velocity scale	(m/s)
V_s	= Slide volume	(m^3)
w	= Channel width	(m)
x	= Surface downslope coordinate	(m)
x_c	= Ramp-wise position of slide mass centroid	(m)
x_f	= Ramp-wise position of slide front	(m)
x_m	= Ramp-wise position of slide peak	(m)
x_r	= Downslope position of end of transition curve	(m)
x_t	= Ramp-wise position of slide tail	(m)
x_1	= First measurement position along channel length	(m)
x_2	= Second measurement position along channel length	(m)
y	= Surface cross-slope coordinate	(m)
z	= Surface normal coordinate	(m)
α	= Reynolds normalization power coefficient	(-)
δ_i	= Ramp bed friction angle	(°)
δ_r	= Runout bed friction angle	(°)
Δt_c	= Rayleigh critical time step	(s)
Δt_s	= Simulation time step	(s)
η_r	= Rolling viscous damping ratio	(-)
λ	= Scale factor	(-)
μ_r	= Rolling-resistance coefficient	(-)
ν_f	= Fluid kinematic viscosity	(m^2/s)
ω_{sh}	= Shutter angular acceleration	(rad/s^2)
ϕ	= Internal friction angle	(°)
ρ_g	= Grain density	(kg/m^3)
θ_i	= Laser incidence angle	(°)
θ_r	= Channel inclination angle	(°)
θ_W	= Release wedge surface angle	(°)

References

Ai, J., Chen, J.-F., Rotter, J. M., & Ooi, J. Y. (2011). Assessment of rolling resistance models in discrete element simulations. *Powder Technology*, *206*(3), 269–282. https://doi.org/10.1016/j.powtec.2010.09.030

Andreotti, B., Forterre, Y., & Pouliquen, O. (2013). *Granular media: Between fluid and solid*, pp. 169–284. Cambridge: Cambridge University Press. https://doi.org/10.1017/CBO9781139541008

Aradian, A., Raphael, E., & de Gennes, P.-G. (2002). Surface flows of granular materials: A short introduction to some recent models. *Comptes Rendus Physique*, *3*(2), 187–196. https://doi.org/10.1016/S1631-0705(02)01304-X

Armanini, A. (2013). Granular flows driven by gravity. *Journal of Hydraulic Research*, *51*(2), 111–120. https://doi.org/10.1080/00221686.2013.788080

Artoni, R., Santomaso, A. C., Go, M., & Canu, P. (2012). Scaling laws for the slip velocity in dense granular flows. *Physical Review Letters*, *108*(23), 1–4. https://doi.org/10.1103/PhysRevLett.108.238002

Bagheri, G., & Bonadonna, C. (2016). On the drag of freely falling non-spherical particles. *Powder Technology*, *301*, 526–544. https://doi.org/10.1016/j.powtec.2016.06.015

Bowman, E. T., Take, W. A., Rait, K. L., & Hann, C. (2012). Physical models of rock avalanche spreading behaviour with dynamic fragmentation. *Canadian Geotechnical Journal*, *49*(4), 460–476. https://doi.org/10.1139/t2012-007

Brodu, N., Delannay, R., Valance, A., & Richard, P. (2015). New patterns in high-speed granular flows. *Journal of Fluid Mechanics*, *769*, 218–228. https://doi.org/10.1017/jfm.2015.109

Bryant, S. K., Take, W. A., & Bowman, E. T. (2014). Observations of grain-scale interactions and simulation of dry granular flows in a large-scale flume. *Canadian Geotechnical Journal*, *52*(5), 638–655. https://doi.org/10.1139/cgj-2013-0425

Campbell, C. S. (2006). Granular material flows—An overview. *Powder Technology*, *162*(3), 208–229. https://doi.org/10.1016/j.powtec.2005.12.008

Choi, C. E., Ng, C. W. W., Au-Yeung, S. C. H., & Goodwin, G. R. (2015). Froude characteristics of both dense granular and water flows in Froude modelling. *Landslides*, *12*(6), 1197–1205. https://doi.org/10.1007/s10346-015-0628-8

Collins, G. S., & Melosh, H. J. (2003). Acoustic fluidization and the extraordinary mobility of sturzstroms. *Journal of Geophysical Research*, *108*(B10), 2473. https://doi.org/10.1029/2003JB002465

Cruden, D. M., & Hungr, O. (1986). The debris of the Frank Slide and theories of rockslide-avalanche mobility. *Canadian Journal of Earth Sciences*, *23*(3), 425–432. https://doi.org/10.1139/e86-044

Cundall, P. A., & Strack, O. D. L. (1979). A discrete numerical model for granular assemblies. *Géotechnique*, *29*(1), 47–65. https://doi.org/10.1680/geot.1979.29.1.47

Davies, T. R., & McSaveney, M. J. (1999). Runout of dry granular avalanches. *Canadian Geotechnical Journal*, *36*(2), 313–320. https://doi.org/10.1139/t98-108

Davies, T. R., McSaveney, M. J., & Hodgson, K. A. (1999). A fragmentation-spreading model for long-runout rock avalanches. *Canadian Geotechnical Journal*, *36*(6), 1096–1110. https://doi.org/10.1139/t99-067

Erismann, T. H. (1986). Flowing, rolling, bouncing, sliding: Synopsis of basic mechanisms. *Acta Mechanica*, *64*(1), 101–110. https://doi.org/10.1007/BF01180101

Ettema, R., Kirkil, G., & Muste, M. (2006). Similitude of large-scale turbulence in experiments on local scour at cylinders. *Journal of Hydraulic Engineering*, *132*(1), 33–40. https://doi.org/10.1061/(ASCE)0733-9429(2006)132:1(33)

Evans, S. G., Hungr, O., & Clague, J. J. (2001). Dynamics of the 1984 rock avalanche and associated distal debris flow on Mount Cayley, British Columbia, Canada; implications for landslide hazard assessment on dissected volcanoes. *Engineering Geology*, *61*(1), 29–51. https://doi.org/10.1016/S0013-7952(00)00118-6

Haque, U., Blum, P., da Silva, P., Andersen, P., Pilz, J., Chalov, S. R., et al. (2016). Fatal landslides in Europe. *Landslides*, *13*(6), 1545–1554. https://doi.org/10.1007/s10346-016-0689-3

Heller, V. (2011). Scale effects in physical hydraulic engineering models. *Journal of Hydraulic Research*, *49*(3), 293–306. https://doi.org/10.1080/00221686.2011.578914

Heller, V. (2017). Self-similarity and Reynolds number invariance in Froude modelling. *Journal of Hydraulic Research*, *55*(3), 293–309. https://doi.org/10.1080/00221686.2016.1250832

Heller, V., Hager, W. H., & Minor, H. E. (2008). Scale effects in subaerial landslide generated impulse waves. *Experiments in Fluids*, *44*, 691–703. https://doi.org/10.1007/s00348-007-0427-7

Hertz, H. (1882). Über die Berührung fester elastischer Körper (on the contact of elastic bodies). *Journal Reine Angewandte Mathematik*, *94*, 156–171. English translation in Miscellaneous Papers by Hertz, H. (ed.) Jones, D. E. and Schott, G. A.

Hutter, K., Koch, T., Plüss, C., & Savage, S. B. (1995). The dynamics of avalanches of granular materials from initiation to runout. Part II. Experiments. *Acta Mechanica*, *109*(1–4), 127–165. https://doi.org/10.1007/BF01176820

Iverson, R. M. (1997). The physics of debris flows. *Reviews of Geophysics*, *35*(3), 245–296. https://doi.org/10.1029/97RG00426

Iverson, R. M. (2015). Scaling and design of landslide and debris-flow experiments. *Journal of Geophysical Research*, *244*, 9–20. https://doi.org/10.1016/j.geomorph.2015.02.033

Iverson, R. M., Logan, M., LaHusen, R. G., & Berti, M. (2010). The perfect debris flow? Aggregated results from 28 large-scale experiments. *Journal of Geophysical Research*, *115*, F03005. https://doi.org/10.1029/2009JF001514

Johnson, B. C., Campbell, C. S., & Melosh, H. J. (2016). The reduction of friction in long runout landslides as an emergent phenomenon. *Journal of Geophysical Research: Earth Surface*, *121*, 881–889. https://doi.org/10.1002/2015JF003751

Juanico, D. E., Longjas, A., Batac, R., & Monterola, C. (2008). Avalanche statistics of driven granular slides in a miniature mound. *Geophysical Research Letters*, *35*, L19403. https://doi.org/10.1029/2008GL035567

Kelfoun, K., Giachetti, T., & Labazuy, P. (2010). Landslide-generated tsunamis at Réunion Island. *Journal of Geophysical Research: Earth Surface*, *115*, F04012. https://doi.org/10.1029/2009JF001381

Kesseler, M. (2019). Laboratory-numerical investigation of scale effects in granular slides (Ph.D. thesis), University of Nottingham, Nottingham. Retrieved from Nottingham ePrints http://eprints.nottingham.ac.uk/59260/2/thesis_091019.pdf

Kesseler, M., Heller, V., & Turnbull, B. (2018). A laboratory-numerical approach for modelling scale effects in dry granular slides. *Landslides*, *15*(11), 2145–2159. https://doi.org/10.1007/s10346-018-1023-z

Kloss, C., Goniva, C., Hager, A., Amberger, S., & Pirker, S. (2012). Models, algorithms and validation for opensource DEM and CFD-DEM. *Progress in Computational Fluid Dynamics*, *12*(2/3), 140–152. https://doi.org/10.1504/PCFD.2012.047457

Körner, H. J. (1977). Flow mechanisms and resistances in the debris streams of rock slides. *Bulletin of the International Association of Engineering Geology*, *16*, 101–104. https://doi.org/10.1007/BF02591460

Kowalczuk, P. B., & Drzymala, J. (2016). Physical meaning of the Sauter mean diameter of spherical particulate matter. *Particulate Science and Technology*, *34*(6), 645–647. https://doi.org/10.1080/02726351.2015.1099582

Kruggel-Emden, H., Rickelt, S., Wirtz, S., & Scherer, V. (2008). A study on the validity of the multi-sphere discrete element method. *Powder Technology*, *188*(2), 153–165. https://doi.org/10.1016/j.powtec.2008.04.037

Lipovsky, P. S., Evans, S. G., Clague, J. J., Hopkinson, C., Couture, R., Bobrowsky, P., et al. (2008). The July 2007 rock and ice avalanches at Mount Steele, St. Elias Mountains, Yukon, Canada. *Landslides*, *5*(4), 445–455. https://doi.org/10.1007/s10346-008-0133-4

Llano-Serna, M. A., Farias, M. M., & Pedroso, D. M. (2016). An assessment of the material point method for modelling large scale run-out processes in landslides. *Landslides*, *13*(5), 1057–1066. https://doi.org/10.1007/s10346-015-0664-4

Markauskas, D., & Kačianauskas, R. (2011). Investigation of rice grain flow by multi-sphere particle model with rolling resistance. *Granular Matter*, *13*(2), 143–148. https://doi.org/10.1007/s10035-010-0196-5

McElwaine, J., & Nishimura, K. (2001). Ping-pong ball avalanche experiments. *Annals of Glaciology*, *32*, 241–250. https://doi.org/10.3189/172756401781819526

McKinnon, M. (2010). Landslide runout, statistical analysis of physical characteristics and model parameters (Ph.D. thesis), University of British Columbia, Vancouver. Retrieved from UBC Theses and Dissertations https://open.library.ubc.ca/cIRcle/collections/ubctheses/24/items/1.0052933

McSaveney, M. J. (2002). Recent rockfalls and rock avalanches in Mount Cook National Park, New Zealand. *Reviews of Engineering Geology*, *15*, 35–70. https://doi.org/10.1130/REG15-p35

Moore, D. P. (1976). The Rubble Creek landslide, Garibaldi, British Columbia (Master's thesis), University of British Columbia, Vancouver. Retrieved from UBC Theses and Dissertations https://open.library.ubc.ca/cIRcle/collections/ubctheses/831/items/1.0052710

Moriwaki, H., Inokuchi, T., Hattanji, T., Sassa, K., Ochiai, H., & Wang, G. (2004). Failure processes in a full-scale landslide experiment using a rainfall simulator. *Landslides*, *1*(4), 277–288. https://doi.org/10.1007/s10346-004-0034-0

Ng, C. W. W., Choi, C. E., Cheung, D. K. H., & Cui, Y. (2018). Effects of dynamic fragmentation on the impact force exerted on rigid barrier: Centrifuge modelling. *Canadian Geotechnical Journal*, *56*(9), 1215–1224. https://doi.org/10.1139/cgj-2018-0092

Ng, C. W. W., Choi, C. E., & Goodwin, G. R. (2019). Froude characterization for unsteady single-surge dry granular flows: Impact pressure and runup height. *Canadian Geotechnical Journal*, *56*(12), 1968–1978. https://doi.org/10.1139/cgj-2018-0529

Nguyen, C. T., Nguyen, C. T., Bui, H. H., Nguyen, G. D., & Fukugawa, R. (2017). A new SPH-based approach to simulation of granular flows using viscous damping and stress regularisation. *Landslides*, *14*(1), 69–81. https://doi.org/10.1007/s10346-016-0681-y

Parez, S., & Aharonov, E. (2015). Long runout landslides: A solution from granular mechanics. *Frontiers in Physics*, *3*(80), 1–10. https://doi.org/10.3389/fphy.2015.00080

Poschel, T. (1993). Granular material flowing down an inclined chute: A molecular dynamics simulation. *Journal de Physique II*, *3*(1), 27–40. https://doi.org/10.1051/jp2:1993109

Pouliquen, O. (1999). Scaling laws in granular flows down rough inclined planes. *Physics of Fluids*, *11*(3), 542–548. https://doi.org/10.1063/1.869928

Pudasaini, S. P., & Hutter, K. (2010). *Avalanche dynamics: Dynamics of rapid flows of dense granular avalanches*. Berlin Heidelberg: Springer-Verlag. https://doi.org/10.1007/978-3-540-32687-8

Ranieri, G. (2007). The surf zone distortion of beach profiles in small-scale coastal models. *Journal of Hydraulic Research*, *45*(2), 261–269. https://doi.org/10.1080/00221686.2007.9521761

Savage, S. B., & Hutter, K. (1989). The motion of a finite mass of granular material down a rough incline. *Journal of Fluid Mechanics*, *199*(1), 177–215. https://doi.org/10.1017/S0022112089000340

Shugar, D. H., & Clague, J. J. (2011). The sedimentology and geomorphology of rock avalanche deposits on glaciers. *Sedimentology*, *58*(7), 1762–1783. https://doi.org/10.1111/j.1365-3091.2011.01238.x

Slonaker, J., Motley, D. C., Zhang, Q., Townsend, S., Senatore, C., Iagnemma, K., & Kamrin, K. (2017). General scaling relations for locomotion in granular media. *Physical Review E*, *95*(5), 1–8. https://doi.org/10.1103/PhysRevE.95.052901

Sosio, R., Crosta, G. B., & Hungr, O. (2008). Complete dynamic modeling calibration for the Thurwieser rock avalanche (Italian Central Alps). *Engineering Geology*, *100*(1–2), 11–26. https://doi.org/10.1016/j.enggeo.2008.02.012

Tavares, L. M., & King, R. P. (1998). Single-particle fracture under impact loading. *International Journal of Mineral Processing*, *54*(1), 1–28. https://doi.org/10.1016/S0301-7516(98)00005-2

Thornton, C. (2015). *Granular dynamics, contact mechanics and particle system simulations*, pp. 13–25. Switzerland: Springer International Publishing. https://doi.org/10.1007/978-3-319-18711-2

Turnbull, B. (2011). Scaling laws for melting ice avalanches. *Physical Review Letters*, *107*(25), 1–4. https://doi.org/10.1103/PhysRevLett.107.258001

Walsh, L. S., Martin, A. J., Ojha, T. P., & Fedenczuk, T. (2012). Correlations of fluvial knickzones with landslide dams, lithologic contacts, and faults in the southwestern Annapurna Range, central Nepalese Himalaya. *Journal of Geophysical Research*, *117*, F01012. https://doi.org/10.1029/2011JF001984

Warnett, J. M., Denissenko, P., Thomas, P. J., Kiraci, E., & Williams, M. A. (2014). Scalings of axisymmetric granular column collapse. *Granular Matter*, *16*(1), 115–124. https://doi.org/10.1007/s10035-013-0469-x

Wensrich, C. M., & Katterfeld, A. (2012). Rolling friction as a technique for modelling particle shape in DEM. *Powder Technology*, *217*, 409–417. https://doi.org/10.1016/j.powtec.2011.10.057

Xu, C., Xu, X., Yao, X., & Dai, F. (2014). Three (nearly) complete inventories of landslides triggered by the May 12, 2008 Wenchuan Mw 7.9 earthquake of China and their spatial distribution statistical analysis. *Landslides*, *11*(3), 441–461. https://doi.org/10.1007/s10346-013-0404-6

Zhang, X., & Vu-Quoc, L. (2000). Simulation of chute flow of soybeans using an improved tangential force–displacement model. *Mechanics of Materials*, *32*(2), 115–129. https://doi.org/10.1016/S0167-6636(99)00043-5

Zhou, G. G. D., & Ng, C. W. W. (2010). Dimensional analysis of natural debris flows. *Canadian Geotechnical Journal*, *47*(7), 719–729. https://doi.org/10.1139/T09-134

Zhu, H. P., Zhou, Z. Y., Yang, R. Y., & Yu, A. B. (2008). Discrete particle simulation of particulate systems: A review of major applications and findings. *Chemical Engineering Science*, *63*(23), 5728–5770. https://doi.org/10.1016/j.ces.2008.08.006